Chimeric identities and reduced stiffness characterise the shoot apex of *Arabidopsis* stem cell mutants

Running title: Properties of stem cell mutants

Léa Rambaud-Lavigne[1,*], Aritra Chatterjee[2,6], Simone Bovio[1,3], Virginie Battu[1], Quentin Lavigne[4], Namrata Gundiah[5,*], Arezki Boudaoud[1,7,*], Pradeep Das[1,*]

[1]Laboratoire Reproduction et Développement des Plantes, Université de Lyon, ENS de Lyon, UCB Lyon 1, CNRS, INRAE, INRIA, Lyon, France. [2]Centre for BioSystems Science and Engineering, Indian Institute of Science, Bengaluru, India. [3]PLATIM-LyMIC, Université de Lyon, ENS de Lyon, Inserm, CNRS, SFR Biosciences US8 UAR3444, UCB Lyon 1, Lyon, France. [4]Physikalisches Institut, Rheinische Friedrich-Wilhelms-Universität, 53115 Bonn, Germany. [5]Department of Mechanical Engineering, Indian Institute of Science, Bengaluru, India.

Present address: [6]Weldon School of Biomedical Engineering, Purdue University, West Lafayette, Indiana, USA. [7]LadHyX, CNRS, Ecole Polytechnique, Institut Polytechnique de Paris, 91128 Palaiseau Cedex, France

[*]Authors for correspondence (lea.rambaud1@ens-lyon.fr, namrata@iisc.ac.in, arezki.boudaoud@polytechnique.edu, pradeep.das@ens-lyon.fr)

ORCID: LRL, 0000-0001-6560-5359; AC, 0000-0002-5318-3459; SB, 0000-0002-9836-6742; VB, 0009-0009-1098-4633; QL, 0000-0003-2326-2604; NG, 0000-0002-9882-5232; AB, 0000-0002-2780-4717; PD, 0000-0002-1179-9044

Key words: shoot apical meristem, *WUSCHEL*, *CLAVATA*, heterogeneities, morphogenesis, stem cell mechanics

Summary statement: Mechanical, genetic and functional evidence supported by theoretical models call into question the current definition of stem cells in the shoot apex.

Abstract

Stem cell homeostasis in the shoot apical meristem involves a core regulatory feedback loop between the signalling peptide CLAVATA3, produced in stem cells, and the transcription factor WUSCHEL, expressed in the underlying organising centre. Compromised CLAVATA activity leads to massive meristem overgrowth, which is thought to be caused by stem cell overproliferation. However, it is unknown how uncontrolled stem cell divisions lead to the specific changes observed in *clavata* mutants. Here we first quantitatively characterise these mutants, to reveal underlying tissue curvature defects. We use analytical models to show how perturbed mechanical properties and/or growth rates may contribute to altered meristem morphology. Indeed, we find that *clavata* meristems are softer than the wild type, and that stereotypical meristem organisation is lost, with cells instead simultaneously expressing multiple domain markers. Furthermore, we show that mutant meristematic cells are auxin-responsive, suggesting that they are functionally different from wild-type stem cells. We propose that the *clavata* phenotype is not caused by stem cell overproliferation, but rather by the disruption of a more complex regulatory framework that is key to maintaining distinct genetic and functional domains at the shoot apex.

Introduction

The shoot apical meristem (SAM) is a structure at the growing tip of the plant that gives rise to all its aboveground tissues. The SAM is sustained by the activity of a small pool of centrally-located undifferentiated stem cells in the slow-dividing central zone (CZ). Through successive divisions, their daughter cells exit from the CZ into the surrounding peripheral zone (PZ), where they may differentiate into lateral organs, such as leaves or flowers. The CZ is itself maintained via the activity of the underlying organising centre (OC) (Laux et al., 1996).

The regulatory network driving stem cell maintenance in *Arabidopsis* is well studied. At its core is a feedback loop between WUSCHEL (WUS), a homeobox transcription factor expressed in the OC, and CLAVATA3 (CLV3), a signalling peptide expressed in the CZ (Brand et al., 2000; Clark et al., 1995; Laux et al., 1996; Schoof et al., 2000). The movement of WUS from the OC to the CZ is necessary for inducing stem cell identity, by directly binding to the *CLV3* promoter and activating its expression (Daum et al., 2014; Yadav et al., 2011). In turn, CLV3 binds receptors such as the leucine-rich-repeat receptor-like kinase CLV1 (Clark et al., 1997), and the receptor-like proteins CLV2 (Kayes and Clark, 1998) and CORYNE (CRN) (Fletcher et al., 1999; Jeong et al., 1999; Miwa et al., 2008; Müller et al., 2008). Signalling from these ligand-receptor complexes ultimately leads to the downregulation of *WUS* in the OC (Miwa et al., 2008; Müller et al., 2006). The absence of WUS activity leads to SAM arrest early in development (Laux et al., 1996), whereas the loss of the *CLV* genes leads to a vast enlargement of the SAM (Clark et al., 1993; Clark et al., 1995; Kayes and Clark, 1998), a phenomenon called fasciation. Several instances of fasciated tissues have been observed in the wild, as well as in crop plants, including beef tomatoes and the maize *fasciated ear2* (*fea2*) mutant (Taguchi-Shiobara, 2001). It is thought that fasciation is caused by stem cell overproliferation in the CZ (Brand et al., 2000; Busch et al., 2010; Dao et al., 2022; Kwon et al., 2005; Lenhard and Laux, 2003; Ma et al., 2019; Müller et al., 2008; Nimchuk et al., 2011; Whitewoods et al., 2018; Wu et al., 2005), or conceivably, by lower rates of cell transit from the CZ to the PZ (Laufs et al., 1998).

Over the years, *CLV3* has been the only known genetic marker to study stem cells at the shoot apex (Müller et al., 2006; Reddy and Meyerowitz, 2005), including for analysing *clv* mutants. While microarray analyses have uncovered several other genes that are enriched in the CZ (Aggarwal et al., 2010; Busch et al., 2010; Yadav et al., 2009), none have been extensively characterised. More recently, atomic force microscopy (AFM) experiments,

which measure cellular mechanical properties, revealed that *CLV3*-expressing cells are stiffer than surrounding PZ cells, and that in flowers, the onset of *CLV3* expression coincides with an increase in cell wall stiffness (Milani et al., 2014). Thus, although stem cell identity is both spatially and temporally associated with increased cell stiffness (Milani et al., 2014), it is unknown how these mechanical patterns are altered when stem cell regulation is perturbed.

The core stem cell regulatory network is also influenced by hormone signalling, including cytokinin and auxin (Gordon et al., 2009; Busch et al., 2010). Exogenous cytokinin treatment phenocopies the *clv* mutant by increasing *WUS* expression and decreasing *CLV1* expression (Lindsay et al., 2006). While exogenous auxin treatment induces organogenesis markers in the PZ, the CZ itself remains unaffected, displaying reduced responsivity to auxin (de Reuille et al., 2006). Whereas in the PZ, the auxin response factor MONOPTEROS (MP) activates the expression of lateral organ identity genes in an auxin-dependent manner (Berleth and Jürgens, 1993; Bhatia et al., 2016; Hardtke and Berleth, 1998; Yamaguchi et al., 2013), it also functions to repress CZ genes that are themselves activators of *CLV3* expression (Luo et al., 2018; Zhao et al., 2010). Despite these advances, it remains unclear how auxin signalling is perturbed in *clv* mutants, and furthermore, whether this plays a direct role in generating the fasciated *clv* phenotype.

In this study, we use quantitative approaches to study the effects of the loss of proper stem cell regulation that reveal hitherto unobserved cellular and tissular phenotypes, such as cell size and local surface curvature in *clv* mutant SAM. We run analytical mechanical models to show that differences in stiffness and/or growth regimes are sufficient to account for the surface curvature defects observed in *clv* mutants. We examine the mechanical properties and genetic identities of *clv* mutant SAM to provide experimental support for these model predictions. Lastly, we show that these differences are correlated with altered sensitivity to auxin.

Results

Altered cellular and tissular properties characterise fasciated *clv* SAM

In order to better understand the defects associated with abnormal stem cell regulation, we first quantified the highly fasciated phenotype of the canonical *clv3-2* allele (Clark et al., 1995). In our growth conditions, shoot meristems in WT plants consistently display a

stereotypical dome shape, whereas *clv3-2* meristems display a highly variable phenotype, most often comprising a large centrally-located bulge from which two or more arm-like outgrowths elongate laterally (Fig. 1A, B). A more detailed analysis using scanning electron microscopy (SEM) reveals that the cellular organisation also varies between the central bulge, which is usually devoid of any discernible organisation, and the lateral arms, which are mostly composed of cell files (Fig. 1C, D). Both the central bulge and the lateral elongations give each SAM a unique aspect, with irregular shapes for the bulge and varying numbers and shapes for the arms (Fig. 1E-G, Fig. S1A).

Previous studies had suggested that cell size in *clv* mutant SAM differs from the WT (Laufs et al., 1998; Schoof et al., 2000). We wondered whether we could use such changes in cellular morphologies to further characterise the mutant phenotypes described above. To quantify cell size, we acquired 3D image stacks of SAM from WT as well as from multiple *clv1* and *clv3* mutant lines. Using only cells at the uppermost regions of the SAM within the image stack, we next extracted slices near the midpoint of cells in the L1 and L2 layers, segmented them using the MorphoGraphX software (Barbier de Reuille et al., 2015) and determined cell areas. We found that across 3 WT SAM, the average cell size is similar in both cell layers, with L1 cells at 23.9 ± 5.83 μm^2 (n = 103) and L2 cells at 24.5 ± 7.18 μm^2 (n = 115) (Fig. 1H). In contrast, L2 cells in *clv3-2* mutants are on average 69% larger than L1 cells – 31.2 $\pm$ 9.84 μm^2 in the L2 versus 18.4 $\pm$ 5.34 μm^2 in the L1 (Fig. 1H). A similar trend was observed for other *clv* alleles, such as *clv1-8* and *clv3-7*, suggesting that altered morphology is a general feature of *clv* mutants. (Fig. S1B).

In order to ensure that the observed changes in cell areas were not imaging artefacts, we next measured cell volumes in WT and *clv3-2* SAM. To this end, we generated 3D reconstructions using the MARS pipeline (Fernandez et al., 2010), which involves acquiring images of samples from multiple angles and fusing them to generate high-resolution images that are then segmented. Consistent with our findings for cell areas, we found that while L1 and L2 cells have similar volumes in the WT (136.51 $\pm$ 40.45 μm^3 and 148.72 $\pm$ 44.54 μm^3, respectively), L2 cells in *clv3-2* SAM are almost twice as large as L1 cells (249.08 $\pm$ 130.65 μm^3 vs 129.48 $\pm$ 40.86 μm^3) (Fig. 1I and Fig. S1C).

An examination of the SEM and confocal images had suggested that meristems in *clv3* mutants are less smooth than WT meristems. One way to better study this is by measuring curvature. To this end, we used a method (Kiss et al., 2017) to precisely detect the outer

surface of the SAM in our high-resolution 3D MARS-reconstructed image stacks, and calculated Gaussian curvature within a 10-μm radius at every pixel of that surface in WT and mutant SAM. We observe stereotypical patterns of local curvature in WT inflorescences, with the SAM and young flowers being homogeneously smooth areas that are separated by boundaries defined by negative curvature (Fig. 1J). In contrast, even the uppermost areas of *clv3-2* SAM, which are distant from the regions where flowers form, display a much more variable surface curvature, with crests and troughs of various sizes distributed throughout the SAM (Fig. 1K). These findings suggest that the arrangement of local curvature that typifies WT meristems is lost in *clv3-2* mutants.

Morphoelastic models reveal how growth and stiffness contribute to surface buckling

To elucidate a theoretical basis for the surface curvature defects of *clv* mutants, we next generated analytical models of SAM development using a growth and remodelling framework (Goriely, 2017). Specifically, we adapted a model developed to explore the biomechanical basis of morphogenesis in systems that display buckling behaviours similar to that observed in *clv* mutants (Almet et al., 2019; Moulton et al., 2013). We modelled the SAM as an axially growing planar elastic rod (the outer L1 layer), attached to an elastic foundation (the inner layers), and clamped at the two ends (Fig. S2). We used the theoretical model to explore how growth stretch, a proxy for tissue growth, and/or mechanical properties, a proxy for cellular stiffness, might contribute to the altered morphology of *clv* mutants (see Supplementary Materials and Methods).

First, we used linear stability analysis to plot output shapes when either only growth stretch (γ) or system stiffness ($\hat{k}$, where *k* is the ratio of foundation and rod stiffnesses) was varied. When the foundation and rod had similar mechanical properties ($\hat{k}$ = 1) and when growth stretch was at a low, subcritical value (γ^*_{inf}= 5.82), the output shape resembled the smooth dome of a WT meristem (Fig. 2A). When growth stretch was raised to a near-critical point (γ^*_{inf}= 8.99), the size of the dome increased, while remaining smooth. A further increase in growth stretch generated various modes of buckling (Fig. 2A) that broadly capture the surface curvature defects of *clv* mutants. Next, we investigated the role of system stiffness ($\hat{k}$) on SAM morphology, while maintaining a background of constant growth stretch (γ^* = 8.99) (Fig. 2B). No buckling was evident for higher values of $\hat{k}$ ($\hat{k}$>1), but when the stiffness was reduced ($\hat{k}$ = 0.5), we observed the appearance of buckling in the rod (Fig. 2B), similar to those obtained using growth values above the critical point (Fig. 2A). Together, these

analytical results indicate that in a biological context, cellular growth and stiffness characteristics could influence tissue architecture of the SAM.

In contrast to the analytical shapes obtained above, *clv* mutant SAM in fact display highly variable local buckling, such that the positions, numbers and amplitudes of folds differ within, and between, individual mutant meristems. We reasoned that such variability could result from heterogeneities in cellular characteristics that generate local differences in growth, stiffness or both. To investigate the effects of local heterogeneities on buckling, we replaced constant growth stretch or system stiffness with one of three distinct functions to generate differential distributions across the rod (Fig. 2C). Indeed, all three functions generate differential buckling over the length of the rod when either growth stretch (Fig. 2D, Fig. S3B-B') or system stiffness (Fig. 2E) is spatially distributed, with the resulting shapes often closely resembling the asymmetry and variable buckling amplitudes visible in sections through various *clv* SAM in the literature. These results suggest that local differences in growth or stiffness within the SAM could explain the phenotypes of *clv* mutants.

Finally, we asked whether variations in system stiffness and growth stretch could act together to generate even greater differences in buckling characteristics. To this end, we used a cosine spatial growth stretch distribution and examined how buckling was affected when system stiffness ($\hat{k}$) was varied between 0.5 and 1.5. We found that for identical distributions of growth, rod buckling varies locally as a function of stiffness (Fig. 2F), suggesting that small changes at the cellular level could alter shape locally.

Taken together, our results indicate that growth and mechanical traits are sufficient to describe the differences in meristem shape between WT and *clv* SAM. Furthermore, local variations of these two parameters could suffice to lead to the local curvature defects observed in *clv* meristems.

Loss of *CLV* activity is associated with a reduction in epidermal cell stiffness

Our models predicted that buckling in *clv* mutants is, at least in part, dependent on stiffness changes in the SAM. We had previously shown that *CLV3*-expressing stem cells are stiffer than PZ cells (Milani et al., 2014). However, because *WUS* expression in the underlying OC is thought to be largely responsible for stem cell identity, and because *WUS* expression expands throughout the L2 of *clv* mutants, it was unclear if cellular stiffness patterns could indeed be altered in the mutant. To test this, we measured rigidity in epidermal cells in WT

and *clv3* SAM using an atomic force microscope (AFM), following the approaches that we developed for WT shoot apices (Milani et al., 2014; Beauzamy et al., 2015). We scanned regions of either 169 μm^2 pixels or 2750 μm^2 using a spherical tip with a radius of 400 nm mounted on a cantilever with a nominal force constant of 42 $N.m^{-1}$. At each point, we applied a force of 1 µN, corresponding to an indentation depth of 100-150 nm, as previously published (Milani et al., 2014). The resulting force-displacement curves were used to calculate the apparent Young's modulus at each point. These values were then corrected in order to remove artefacts caused by local slope, particularly in *clv* mutant SAM (Fig. 3A-D). We found that cells in WT SAM displayed an apparent Young's modulus of 12.16 $\pm$ 1.17 MPa (mean $\pm$ s. d.). On the other hand, *clv3-2* mutant SAM have an average apparent Young's modulus of 9.63 $\pm$ 0.74 MPa, indicating that these cells are significantly softer than the WT (Fig. 3E, Fig. S4). Similarly, compared to WT Col-0 plants, *clv1-8* meristems also display significantly lower apparent Young's moduli (Col-0: 10.58 $\pm$ 0.38 MPa, *clv1-8*: 8.94 $\pm$ 0.45 MPa) (Fig. 3E, Fig. S4, Table S1). These results are consistent with those from our analytical models, which suggest that reduced tissular stiffnesses can result in buckling, hence in surface curvature defects.

Functional domain separation is absent in *clv* SAM

We reasoned that the local heterogeneities in growth and/or stiffness, as predicted by our models, might be caused by variations in local genetic identity in cells of *clv* shoot apices. While no previous studies have suggested that this is the case, neither did those studies specifically examine *clv* meristems for such differences. To determine whether such variations do indeed exist, we started by retesting the expression patterns of CZ and OC markers using mRNA *in situ* hybridisation assays in WT and *clv3* mutant SAM. To examine CZ identity, we tested several genes that had been identified as enriched in *CLV3*-expressing cells (Yadav et al., 2009). We settled on the *APUM10* gene that encodes a protein of the Puf family, whose conserved Pumillio homology domain regulates mRNA stability and translation in eukaryotic cells, via its sequence-specific RNA binding (Tam et al., 2010; Abbasi et al., 2011; Qiu et al., 2019). The precise function of APUM10 is unknown. We used *WUS* to examine OC identity (Laux et al., 1996; Mayer et al., 1998).

APUM10 is expressed in an approximately 8-cell domain at the centre of the SAM (Fig. 4A), and *WUS* is expressed in an underlying group of cells (Fig. 4C). As expected in *clv3-2* mutant SAM, we detect both *APUM10* and *WUS* in a broad domain occupying almost the entire meristem, with *APUM10* expressed principally in the L2 layer (Fig. 4B, B'), while *WUS*

is expressed in deeper layers (Fig. 4D, D'). However, both genes are expressed in a discontinuous manner, with patches of cells throughout the SAM not displaying any detectable expression (Fig. 4B, D). A close inspection of similar work published by other groups shows that such a patchy expression was visible, but had gone unnoticed (Brand et al., 2000; Schuster et al., 2014).

It was unclear to us why some patches of cells in a *clv3* mutant might not express stem cell or OC identity. We reasoned that such cells might instead express PZ markers. To test this, we localised mRNA for the *MP* gene, which is expressed mainly in the PZ in the WT (Hardtke and Berleth, 1998; Zhao et al., 2010) (Fig. 4E). In enlarged *clv3-2* SAM, the PZ is thought to be restricted to areas adjacent to the flowers, well below the top of the SAM. However our data reveal that in *clv* mutants, *MP* expression is also very broad, similar to the expression patterns of the CZ and OC markers (Fig. 4F, F'). Strikingly, we also noted that patches of cells are devoid of *MP* expression (Fig. 4F'). Taken together, our results suggest that identities of the three key SAM zones are present in overlapping groups of cells in *clv3-2* SAM. Furthermore, they are expressed discontinuously in the sub-epidermal cell layer, which gives an impression of an overall patchiness. In short, the expression patterns of *APUM10*, *MP*, and *WUS* are overlapping and do not set clear boundaries between functional domains of the *clv3-2* SAM. They are rather patchy and spanning all over the enlarged SAM.

Because our results seemingly contradicted the prevailing view of *clv3* SAM being composed entirely of stem cells (Brand et al., 2002; Busch et al., 2010; Dao et al., 2022; Kwon et al., 2005; Lenhard and Laux, 2003; Ma et al., 2019; Müller et al., 2006; Nimchuk et al., 2011; Whitewoods et al., 2018; Wu et al., 2005), we thought it possible that normal domain organisation might exist at a more local level. In order to more closely investigate the relative positioning of *APUM10*, *MP*, and *WUS* expression domains in *clv3* SAM, we performed pairwise *in situ* hybridisations using alternating serial sections, with one probe used on even-numbered sections, and the other on odd-numbered sections. Our results indicate that in the WT, *APUM10* and *WUS* expression domains do not appear to overlap, because *APUM10* is detected in the outer cell layers of the CZ whereas *WUS* is expressed in deeper cells (Fig. 4G, G'). However in the *clv3-2* mutant, the expression domains largely overlap across the entire SAM (Fig. 4H-I', Fig. S5), with a few zones where *APUM10* is expressed and *WUS* is not (Fig. 4H', I'). Similarly, in the WT, *APUM10* and *MP* are expressed in the mutually exclusive CZ and PZ domains, respectively (Fig. 4J, J'), whereas in the *clv3-2* mutant, they are frequently observed together in cells of the SAM. However,

we sometimes detected patches of cells displaying only *MP* expression, as well as patches of cells devoid of any signal of these genes (Fig. 4K-L', Fig. S6). Together, these results show that *clv3* SAM comprise a heterogeneous group of cells with mixed genetic identities, rather than a homogeneous population of stem cells resembling the cells located above the WT OC. Furthermore, we observed similar expression patterns in SAM from other alleles of *clv1* and *clv3* (Fig. S7), suggesting that chimeric cell identities are a general feature of fasciated *clv* meristems.

Exogenous auxin elicits a strong response throughout the *clv3* meristem

Given that cells in fasciated *clv3* SAM show traits not usually associated with stem cells, such as chimeric cell identities, and reduced stiffness, we wondered if they are also functionally different from stem cells. We wished to use auxin response as a functional test in *clv* mutants for the following reasons. First, it has long been thought that a key aspect of organogenesis at the shoot apex is the presence of a CZ that is insensitive to auxin signalling (de Reuille et al., 2006; Douady and Couder, 1996; Galvan-Ampudia et al., 2020; Vernoux et al., 2011). Thus auxin insensitivity could conceivably be used as a readout for cell identity in the SAM. Secondly, anecdotal evidence indicates that unlike WT plants, *clv3* mutants grown in the presence of the auxin transport inhibitor N-1-naphthylphthalamic acid, never show escapers that form lateral organs (O. Hamant and T. Vernoux, personal communication), suggesting an interaction between the CLV and auxin pathways. Lastly, recent work has shown that MP regulates the polar subcellular localisation of the PIN1 auxin efflux transporter, which promotes auxin accumulation and drives organogenesis (Bhatia et al., 2016). Since *MP* is misregulated in *clv* mutants, it is possible that auxin fluxes are perturbed and that organogenesis is affected.

In order to directly test how *clv3* shoot apices respond to auxin, we treated WT and *clv3-2* SAM with exogenous auxin for 5 hours as described (Galvan-Ampudia et al., 2020), and observed the expression of the *pDR5rev::GFPer* auxin signalling reporter approximately 7 and 25 hours after the start of treatment. In WT samples prior to treatment, *DR5* expression is visible in the L1 of the SAM, but not in the CZ (Fig. 5A, D). 7 h after the end of auxin treatment, WT SAM display moderate GFP expression in large portions of the PZ and in internal layers, with no expression observed in the CZ (Fig. 5B, E). At 25 h, we observed high levels of GFP throughout the PZ and in internal layers, and almost none in the CZ (Fig. 5C, F). Similar results are observed in floral meristems, with high expression in the PZ and in internal layers, and none in the CZ (Fig. 5B-C, E-F). In untreated *clv3-2* samples, *DR5*

expression was different from the WT, in that we detected no GFP in the bulk of the enlarged SAM, with the exception of a few L1 cells (Fig. 5G, J, M, P). After treatment with auxin, *clv3* mutants responded in one of two ways. In the first group (n = 4 out of 6) *DR5* expression in the SAM was increased in the inner layers, but not in the L1 at 6 h (Fig. 5H, K), and this trend was further enhanced at 25 h (Fig. 5I-L). In the second group (n = 2 out of 6), we observed a mild increase in *DR5* expression in the SAM at 6 h (Fig. 5N, Q), whereas at 25 h, high GFP expression was detected throughout the SAM (Fig. 5O, R). In *clv3* flowers prior to treatment, small patches of *DR5* expression were observed, whereas after treatment, high levels of expression were detected throughout all floral meristems, with no evident zone of exclusion representing a putative CZ, as in the WT (Fig. 5M-O). Taken together, these results show that cells in *clv* mutant SAM are capable of responding to auxin signalling, an output more associated with WT PZ, rather than CZ, cells. These data also indicate that auxin distribution and/or the capacity for proper auxin signalling are disrupted in fasciated *clv* SAM.

Discussion

The loss of *CLV* activity in *Arabidopsis* shoot apical stem cells leads to the development of fasciated meristems, a phenotype broadly interpreted as being caused by a massive increase in stem cell numbers. Direct experimental evidence for this, as far as we can ascertain, comes from a *CLV3* transcriptional reporter (Brand et al., 2002; Reddy and Meyerowitz, 2005) that is expressed throughout the enlarged meristem of *clv3* mutants. However, given that WUS is broadly expressed throughout the L2 of *clv* mutants, that it is sufficient to activate *CLV3* expression (Schoof et al., 2000), and that it does so by directly binding the *CLV3* promoter (Yadav et al., 2011), it is unsurprising that a *CLV3* transcriptional reporter would be broadly expressed in *clv* meristems. Thus the *CLV3* reporter is not an appropriate marker to study cell identity in *clv* mutants.

An alternate way of deciphering regional identities in *clv* mutants is by characterising cellular properties. One study suggested that *clv* L1 cells are slightly smaller than the WT, while L2 cells are slightly larger (Laufs et al., 1998), while another hinted that *clv* L1 cells are likely larger than the WT (Schoof et al., 2000). However, that analysis was based on inter-nuclear distances and only provided a rough estimate of cell size. In this manuscript, we use more recently-developed approaches (Fernandez et al., 2010; Barbier de Reuille et al., 2015; Kiss et al., 2017) to quantify cell volumes, areas and surface curvatures. Our findings show that

the size of subepidermal cells in *clv* mutant SAM are much larger than in the WT, and resemble certain WT L3 cells, such as those in the potential OC (Fernandez et al., 2010). Curiously, this observation is reminiscent of previous findings that floral meristems lack one of the two layers of the tunica with respect to the SAM (Popham, 1951). The effect of this volume change in L2 cells on meristem structure is difficult to estimate. One possibility is that the abrupt change in cell size generates a higher frequency of cell boundary overlaps between the L1 and L2, which in turn could create a more fragile structure, akin to building a wall with smaller cells in one layer and much larger bricks in the next. The tissue buckling we observe could be located around such regions.

Over the past 15 years, several groups have generated reaction-diffusion or other biochemical computational models to study how a stable CLV-WUS feedback pattern is maintained in the SAM (Jönsson et al., 2005; Jönsson et al., 2006; Fujita et al., 2011; Chickarmane et al., 2012; Gruel et al., 2016; Klawe et al., 2020; Plong et al., 2021; Battogtokh and Tyson, 2022). However, because these studies were mostly carried out in the absence of cell division rules, they have not needed to address the mechanical constraints created by growth. Similarly, models of phyllotaxis at the shoot apex have also mostly favoured addressing how purely biochemical events underlie the distinct auxin accumulation patterns that lead to organogenesis (Reinhardt et al., 2000; Vernoux et al., 2000; Heisler et al., 2005; Galvan-Ampudia et al., 2020). Our analytical model, on the other hand, attempts to explain morphology through a mechanical framework. The model shows that differences in mechanical properties, alone or in combination with differences in growth rates, can explain tissue buckling. Furthermore, local mechanical or growth heterogeneities are sufficient to describe the buckling phenotypes of *clv* SAM.

Certain *clv* alleles do not display the line fasciation exhibited by alleles used in this study, but instead exhibit point fasciation, a milder phenotype where the SAM is a broader and taller dome with respect to the wild type (Clark et al., 1993; Laufs et al., 1998; Schoof et al., 2000). Our modelling analyses indicate that when growth is only slightly increased, the resulting phenotype is one of tissue bulging without significant buckling (Fig. 2A curve for γ^* = 8.99). In this manner, a weaker *clv* allele, or indeed a single mutant as compared to a multiple knock-out (Dao et al., 2022), might impose a lower increase in cellular growth rate that, when combined with sufficient residual stiffness, could temper the phenotype by preventing massive overproliferation, thus leading to a less dramatic fasciation than the stronger alleles examined in this study.

One specificity in our models is that we do not directly address absolute cell stiffness in the different layers, but rather utilise a ratio of stiffness between the inner and outer layers to examine system behaviour. Because it is currently challenging to ascertain cell stiffness in inner layers, we cannot directly confront our model. However, stiffness can be measured with some accuracy in the outer layer. Because the literature suggests that all L1 cells in *clv* SAM have stem cell identity, and because *CLV3*-expressing cells are stiffer than PZ cells, we had predicted that L1 cells in the enlarged *clv* SAM would display higher stiffness compared to WT cells. However, our measurements showed that *clv* L1 cells are consistently less stiff than the WT. Our results thus indicate that cells in *clv* SAM are qualitatively different to those found in the CZ or PZ of wild-type SAM.

A recent study has revealed a link between the number of neighbours for any given cell (neighbour number) and cell size, and how they influence tissue patterning (Long et al., 2020), showing that turgor pressure is anticorrelated to cell size and neighbour number, and that pressure correlates with growth. Thus smaller cells tend to have fewer neighbours, and display lower pressure and higher growth. Therefore the larger cells of the L2 layer of *clv* mutants might be less stiff than the L1, which is itself less stiff than the CZ or PZ of the WT. This is consistent with the predictions from our analytical models, which suggest that buckling occurs when the inner layers are less stiff than the L1 (Cao and Hutchinson, 2012; Cerda and Mahadevan, 2003). An experimental validation of this would require the use of techniques to measure stiffness or pressure in internal layers.

Several articles have revealed that tissue-level shape robustness emerges from cell growth and size variability averaged through space and time (Hervieux et al., 2016; Hong et al., 2016; Kamimoto et al., 2016; Tsugawa et al., 2017; Long et al., 2020). The local mechanical and growth heterogeneities predicted by our models are likely to be principally caused by perturbed genetic patterns in *clv* mutants. Our results show that unlike in WT SAM, which display a clear separation of functional domains and associated gene expression patterns, cells in *clv* SAM bear identities that are chimeric and variable. Cells in *clv* SAM display various abnormal combinations of CZ, OC and PZ identity, with each of them expressed non-uniformly within the meristem. This patchiness is visible in certain mRNA *in situ* localisation data on *clv* SAM in the literature (Brand et al., 2000; Schoof et al., 2000; Reddy and Meyerowitz, 2005; Schlegel et al., 2021), but has not been accorded much importance.

It is unclear precisely how such a mixed pattern arises and what the exact consequences might be.

We propose that cell function is differentially regulated in cells with differing chimeric identities, leading to varying growth or mechanical properties, which in turn alter morphogenesis at the tissue level. Our data suggest that the bulk of the cells in *clv* SAM are in fact capable of responding to exogenous auxin treatment, which resembles the behaviour of PZ, rather than CZ, cells. However, these chimeric *clv* cells clearly do not undergo differentiation. Because the tight regulation of auxin accumulation in space and time is crucial for proper organogenesis (Reinhardt et al., 2000; Vernoux et al., 2000; Heisler et al., 2005; Galvan-Ampudia et al., 2020), one possibility is that auxin regulation is also perturbed in *clv* SAM. It may be that the abnormal shape of the mutant SAM does not allow proper auxin accumulation patterns to be generated. Alternatively, CLV signalling could regulate auxin activity more directly, such as in the moss (Nemec-Venza et al., 2022). A detailed analysis of auxin fluxes and auxin signalling, particularly during vegetative growth in *clv* mutants, will be essential for a full understanding of the role of auxin in fasciation.

Taken together, our data strongly suggest that cells in fasciated *clv* meristems do not fit the current definition of true stem cells. Alternatively, it is possible that cellular identities in mutants with perturbed stem cell regulation are fluid. It could also be that such fluid or chimeric identities also exist in the wild type, for instance at CZ-PZ or PZ-flower boundaries. It is possible that our current definition of stem cells is too restrictive, and needs to be expanded to include not only genetic, but also mechanical and functional parameters. Better reporters for diverse cellular properties, as well as a detailed real-time analysis, will be necessary to resolve how such chimeric identities arise and what their effects are on plant architecture.

Materials and methods

Plant material and culture conditions

The following plant lines were used in this study: L*er* and Col-0 as wild types, *clv3-2* (Clark et al., 1995), *clv3-7* (Fletcher et al., 1999), *clv1-8* (Medford et al., 1992), *pCLV3::GFPer* (Reddy and Meyerowitz, 2005), *pDR5rev::GFPer* (Friml et al., 2003), *pDR5::3xVENUS-N7* (Vernoux et al., 2011), and *pUBQ10::LTI6b-TdTomato* (Shapiro et al., 2015).

Seeds were sown on soil, and placed in short-day conditions (8 hrs light, 20°C, 50-60% humidity and 16 hrs dark, 16°C, 50-60% humidity) for ten days. Seedlings were then transplanted into individual pots and placed back into the short-day conditions growth chamber. One month after transplantation, plants were transferred from short-day to long-day conditions (16 hrs light period, 20°C, 60% humidity and 8 hrs dark period, 19°C, 60% humidity) until flowering. The light sources were LED fixtures (Valoya, C75, spectrum NS12), with an intensity of 150 $\mu mol.m^{-2}.s^{-1}$.

RNA in situ hybridisations

RNA *in situ* hybridisations on sections were performed according to published protocols (Long et al., 1996). Dissected meristems were fixed in FAA (formaldehyde 3.7% [v/v], ethanol 50% [v/v], acetic acid 5% [v/v], H_2O to final volume), washed, dehydrated and embedded in paraplast. Embedded samples were cut (10 µm-thick) and attached to pre-coated glass slides (Superfrost Plus Gold, Fisher Scientific). Antisense probes were made from PCR products using cDNA from inflorescences as a template, except for *CLV3*, which was amplified using genomic DNA. Those PCR products were transcribed into RNA and then labelled using digoxigenin (DIG)-UTP. All probes were filtered on columns (CHROMA SPIN-30 columns, Clontech) to remove remaining nucleotides. Immunodetection was performed using an anti-DIG antibody coupled to alkaline phosphatase (Anti-Digoxygenin-AP, Fab fragments), whose activity was detected by the chromogenic method using NBT/BCIP (Roche). Sections were finally washed with water and observed under a Zeiss Imager M2 microscope equipped with an AxioCam Mrc camera, and 10 X or 20 X objectives in DIC (differential interference contrast) mode.

Plant dissection and preparation for confocal microscopy

SAM were grown on soil and dissected soon after bolting. An approximately 1 cm region at the apex of the stem was placed in apex culture medium (ACM: ½ MS medium, 1% [w/v] sucrose, pH adjusted to 5.8 with 1M KOH, 0.8% [w/v] agarose, supplemented with 1X vitamins (1000X stock: 5 g myo-inositol, 0.05 g nicotinic acid, 640.05 g pyridoxine hydrochloride (B6), 0.5 g thiamine hydrochloride (B1), 0.1 g glycine, H_2O to 50 mL, filter before aliquoting) and cytokinins (BAP; 125-175 nM final)), and flower buds were removed until the shoot meristem was sufficiently exposed for proper imaging. Dissected samples were placed in a growth cabinet under long-day conditions until confocal observation.

Confocal imaging

Imaging was carried out on a Leica TCS SP8 (DM6000 CS) upright confocal laser scanning microscope, equipped with a 25x water dipping lens (Leica HC FLUOTAR L 25x/0.95 W VISIR) and a Leica HyD hybrid detector. FM4-64 (ThermoFisher Scientific, T13320) was used to mark the plasma membrane as previously described (Fernandez et al., 2010). It was excited with a 488 nm laser diode and detected at 600-640 nm. GFP was excited at 488 nm and detected at 500-520 nm. VENUS was excited at 514 nm and detected at 520-535 nm. tdTomato was excited at either 514 or 552 nm and detected at 560-600 nm.

Image analysis

Confocal images were analysed with Fiji (Schindelin et al., 2012). Fiji was used to generate 2D projections from 3D confocal stacks (3D viewer plugin) and to generate orthogonal slices.

3D reconstructions of confocal stacks were generated using the MARS pipeline (Fernandez et al., 2010). Shoot meristems were imaged from three or four different angles by means of a custom-made device to tilt and/or rotate the sample by 15-20 degrees between acquisitions. These images were then fused using MARS and the external contours of the sample were detected using the Level Set Method (Kiss et al., 2017). This contour, along with the 3D reconstructed sample to generate cell-segmented images in 3D using a watershed segmentation algorithm. Cells were then extracted from the segmented image for the L1 and L2 tissue layers and the volume of each cell was calculated.

Cell area measurements

Cell areas were extracted by analysing individual image stacks, focussing on the region of the tissue orthogonal to the axis of the image. We determined the midline of the small group of cells within each layer near the centre of the image. These individual slices were then segmented and cell areas determined using MorphoGraphX (Barbier de Reuille et al., 2015; Kiss et al., 2017). We finally used R to plot the data and run statistical tests.

Computation of SAM curvature

Tissue surface curvature measurements were made using MorphoGraphX (MGX) (Barbier de Reuille et al., 2015; Kiss et al., 2017). The LSM contour for each 3D MARS-reconstructed sample (see above) was used to first generate a mesh and the Gaussian curvature was calculated for a 10-pixel radius for each pixel in the image.

Statistical analysis

Plots and statistical analyses were done in the R environment (Posit team, 2023). Welch's t-tests were used to compare the mean of two independent groups: cell areas and cell volumes in different cell layers, and the apparent Young's modulus in WT and mutant SAM. When we use boxplots, the boxes extend from the first to the third quartile and the whiskers from 10% to 90% of the values, the solid black line represents the median of the distribution. Throughout the manuscript, average values are means $\pm$ s.d.

Hormone treatments

Auxin treatments were performed by immersing dissected SAM into 1mM Indole-3-acetic acid (IAA) solution (Sigma, 0.2 M IAA stock, extemporaneously diluted 1:200 in H_2O). For consistency, the treatment was started prior to 7.30 A.M. and lasted for five hours as described (Galvan-Ampudia et al., 2020). The IAA solution was changed midway. Samples were then imaged by confocal microscopy five, 12 and 30 hours post-treatment to follow DR5 reporter expression dynamics.

Analytical models

See supplementary methods.

Atomic force microscopy (AFM) and data analysis

The day before the experiment, SAM were dissected to remove all flower buds older than stage 3 that hindered access to the meristem. The samples were placed into 50 mm plastic Petri dishes filled with ACM, and grown overnight in a growth cabinet with long-day conditions. SAM were stained with FM4-64 and imaged with a Leica TCS SP8 (DM600 CS) upright confocal laser scanning microscope to collect cell contours.

AFM experiments were performed on a stand-alone JPK Nanowizard III microscope equipped with a CellHesion module and a 100 µm-range Z piezo driven by a JPK Nanowizard software 6.0. The acquisitions were done in Quantitative Imaging mode (QI). The experiments were performed in distilled water at room temperature. We used a silica spherical tip (Special Development SD-sphere-NCH, Nanosensors) mounted on a silicon cantilever with a nominal force constant of 42 $N.m^{-1}$, and a radius of 400 nm. Scan size was generally within 45 and 60 µm (even if in one case we went up to 80 µm, but smaller scans are faster and prevent growth to impact the imaging) with pixel size of approximately 500

nm (e.g. 96 x 96 pixels for 45 µm scan size). The applied force trigger was 1 µN, a force corresponding to 100-150 nm indentation, in order to indent the cell wall only (Milani et al., 2011; Tvergaard and Needleman, 2018). The ramp size was 2 µm, approach speed was 10 $\mu m.s^{-1}$ and retraction speed 100 $\mu m.s^{-1}$.

Cantilever calibration was performed following the standard thermal noise method. We measured the deflection sensitivity by doing a linear fit of the contact part of a force curve acquired on sapphire in phosphate-buffered saline (PBS). Then, we determined the spring constant by acquiring the thermal noise spectrum of the cantilever and fitting the first normal mode peak using a single harmonic oscillator model. The same tip was used for several experiments in different days as long as possible. In order to reduce the offsets in force that can be introduced by each new calibration, especially by the measurements of the deflection sensitivity, we followed the SNAP protocol (Schillers et al., 2017).

Data analysis was done using JPK Data Processing software 6.0. Force vs height curves were first flattened by removing the result of a linear fit done over a portion of the baseline, in order to set this part to 0 force. A first estimation of the point of contact (POC), was obtained considering the first point crossing the 0 of forces, starting from the end of the approach curve (i.e. trigger force position). The force vs. tip-sample distance was then obtained calculating a new axis of distances as Height [m] – tip deflection Δz [m]. Young's modulus was obtained by fitting the entire force vs tip-sample distance curves (note that we used approach curves) with a Hertz model (referred to as Paraboloid in JPK Data Processing). For our analysis, we used a tip radius R of 400 nm and a Poisson's ratio v of 0.5 (as it is conventionally set for biological material in the literature (Kulkarni et al., 2018)), where the Young's modulus, the POC and an offset in force were kept as free parameters of the fit. A preliminary filtering step was performed to exclude data points associated with α, the angle between the normal to the surface and the z direction, superior or equal to 55°. This threshold was set based on the distribution of angles in all samples. In addition, a non systematic second filtering step was applied on samples containing artefacts on their surface, such as dust particles. The threshold criteria aims at removing data that are not well processed by the Hertz model. Thus, the data with the 10% highest residuals root mean square values were excluded.

Finally, we removed or reduced the effect of the local slope in our calculations by adapting a formula from the literature (Routier-Kierzkowska et al., 2012), thus leading to the following corrected apparent Young's modulus equation:

572 $$E_n = E_z(1 + p^2)^{\frac{5}{4}}, (1).$$

573 With E_n the corrected apparent Young's modulus in the direction normal to the surface, E_z
574 the Young's modulus in the z direction, and $p = tan(\alpha)$, with α being the angle between the
575 normal to the surface and the z direction.
576

577 **Acknowledgements**

578 We thank V. Mirabet and N. Dubrulle for help with preliminary AFM measurements, A. Kiss
579 for help with 3D segmentations and surface curvature detection, and G. Gilbert for help with
580 *in situ* hybridisations. We thank the PLATIM/LyMIC imaging facility of the SFR Biosciences
581 (UMS3444/CNRS, US8/Inserm, ENS de Lyon, UCBL1). We thank A. Lacroix, J. Berger, P.
582 Bolland, H. Leyral, and I. Desbouchages for assistance with plant growth and logistics. This
583 article is based on LRL's PhD thesis: Rambaud-Lavigne, L. E. S. (2018), The genetics and
584 mechanics of stem cells at the Arabidopsis shoot apex. *PhD thesis*, University of Lyon, Lyon,
585 France, downloadable at: theses.hal.science/tel-02366972.
586

587 **Author contributions**

588 Conceptualization: LRL, AB, PD; Methodology: AC, NG, SB, AB; Software & Modeling: AC,
589 NG; Validation: LRL, VB, PD; Formal Analysis: QL, AC, LRL, PD; Investigation: LRL, SB,
590 VB, PD; Data Curation: LRL, PD; Writing - Original Draft Preparation: LRL, AC, NG, PD;
591 Writing - Review & Editing: LRL, AC, SB, NG, AB, PD; Visualisation: LRL, AC, QL, NG, PD;
592 Supervision: NG, AB, PD; Funding Acquisition: LRL, NG, PD.
593

594 **Competing interests**

595 No competing interests declared.
596

597 **Funding**

598 This work was supported by a PhD fellowship from the Ecole Normale Supérieure de Lyon
599 (ENSL) to LRL., and a Science Engineering Research Board grant (SERB-POWER) to NG.
600

601 **Data availability**

602 All datasets and scripts will be made available before publication.

References

Abbasi, N., Park, Y.-I. and Choi, S.-B. (2011). Pumilio Puf domain RNA-binding proteins in Arabidopsis. *Plant Signal. Behav.* **6**, 364–368.

Aggarwal, P., Yadav, R. K. and Reddy, G. V. (2010). Identification of novel markers for stem-cell niche of Arabidopsis shoot apex. *Gene Expr. Patterns* **10**, 259–264.

Barbier de Reuille, P., Routier-Kierzkowska, A.-L., Kierzkowski, D., Bassel, G. W., Schüpbach, T., Tauriello, G., Bajpai, N., Strauss, S., Weber, A., Kiss, A., et al. (2015). MorphoGraphX: A platform for quantifying morphogenesis in 4D. *eLife* **4**, 05864.

Battogtokh, D. and Tyson, J. J. (2022). Nucleation of stem cell domains in a bistable activator-inhibitor model of the shoot apical meristem. *Chaos Woodbury N* **32**, 093117.

Beauzamy, L., Louveaux, M., Hamant, O. and Boudaoud, A. (2015). Mechanically, the Shoot Apical Meristem of Arabidopsis Behaves like a Shell Inflated by a Pressure of About 1 MPa. *Front. Plant Sci.* **6**,.

Berleth, T. and Jürgens, G. (1993). The role of the monopteros gene in organising the basal body region of the Arabidopsis embryo. *Development* **118**, 575–587.

Bhatia, N., Bozorg, B., Larsson, A., Ohno, C., Jönsson, H. and Heisler, M. G. (2016). Auxin Acts through MONOPTEROS to Regulate Plant Cell Polarity and Pattern Phyllotaxis. *Curr. Biol.* **26**, 3202–3208.

Brand, U., Fletcher, J. C., Hobe, M., Meyerowitz, E. M. and Simon, R. (2000). Dependence of Stem Cell Fate in Arabidopsis on a Feedback Loop Regulated by CLV3 Activity. *Science* **289**, 617–619.

Brand, U., Grünewald, M., Hobe, M. and Simon, R. (2002). Regulation of CLV3 Expression by Two Homeobox Genes in Arabidopsis. *Plant Physiol.* **129**, 565–575.

Busch, W., Miotk, A., Ariel, F. D., Zhao, Z., Forner, J., Daum, G., Suzaki, T., Schuster, C., Schultheiss, S. J., Leibfried, A., et al. (2010). Transcriptional Control of a Plant Stem Cell Niche. *Dev. Cell* **18**, 841–853.

Cao, Y. and Hutchinson, J. W. (2012). Wrinkling Phenomena in Neo-Hookean Film/Substrate Bilayers. *J. Appl. Mech.* **79**,.

Cerda, E. and Mahadevan, L. (2003). Geometry and Physics of Wrinkling. *Phys. Rev. Lett.* **90**, 074302.

Chickarmane, V. S., Gordon, S. P., Tarr, P. T., Heisler, M. G. and Meyerowitz, E. M. (2012). Cytokinin signaling as a positional cue for patterning the apical–basal axis of the growing Arabidopsis shoot meristem. *Proc. Natl. Acad. Sci. U. S. A.* **109**, 4002–4007.

Clark, S. E., Running, M. P. and Meyerowitz, E. M. (1993). CLAVATA1, a regulator of meristem and flower development in Arabidopsis. *Development* **119**, 397–418.

Clark, S. E., Running, M. P. and Meyerowitz, E. M. (1995). CLAVATA3 is a specific regulator of shoot and floral meristem development affecting the same processes as CLAVATA1. *Development* **121**, 2057–2067.

Clark, S. E., Williams, R. W. and Meyerowitz, E. M. (1997). The CLAVATA1 gene encodes a putative receptor kinase that controls shoot and floral meristem size in Arabidopsis. *Cell* **89**, 575–585.

Dao, T. Q., Weksler, N., Liu, H. M.-H., Leiboff, S. and Fletcher, J. C. (2022). Interactive CLV3, CLE16 and CLE17 signaling mediates stem cell homeostasis in the Arabidopsis shoot apical meristem. *Development* **149**, dev200787.

Daum, G., Medzihradszky, A., Suzaki, T. and Lohmann, J. U. (2014). A mechanistic framework for noncell autonomous stem cell induction in Arabidopsis. *Proc. Natl. Acad. Sci.* **111**, 14619–14624.

de Reuille, P. B., Bohn-Courseau, I., Ljung, K., Morin, H., Carraro, N., Godin, C. and Traas, J. (2006). Computer simulations reveal properties of the cell-cell signaling network at the shoot apex in Arabidopsis. *Proc. Natl. Acad. Sci. U. S. A.* **103**, 1627–1632.

Douady, S. and Couder, Y. (1996). Phyllotaxis as a Dynamical Self Organizing Process Part II: The Spontaneous Formation of a Periodicity and the Coexistence of Spiral and Whorled Patterns. *J. Theor. Biol.* **178**, 275–294.

Fernandez, R., Das, P., Mirabet, V., Moscardi, E., Traas, J., Verdeil, J.-L., Malandain, G. and Godin, C. (2010). Imaging plant growth in 4D: robust tissue reconstruction and lineaging at cell resolution. *Nat. Methods* **7**, 547–553.

Fletcher, J. C., Brand, U., Running, M. P., Simon, R. and Meyerowitz, E. M. (1999). Signaling of Cell Fate Decisions by CLAVATA3 in Arabidopsis Shoot Meristems. *Science* **283**, 1911–1914.

Friml, J., Vieten, A., Sauer, M., Weijers, D., Schwarz, H., Hamann, T., Offringa, R. and Jürgens, G. (2003). Efflux-dependent auxin gradients establish the apical–basal axis of Arabidopsis. *Nature* **426**, 147–153.

Fujita, M., Himmelspach, R., Hocart, C. H., Williamson, R. E., Mansfield, S. D. and Wasteneys, G. O. (2011). Cortical microtubules optimize cell-wall crystallinity to drive unidirectional growth in Arabidopsis. *Plant J.* **66**, 915–928.

Galvan-Ampudia, C. S., Cerutti, G., Legrand, J., Brunoud, G., Martin-Arevalillo, R., Azais, R., Bayle, V., Moussu, S., Wenzl, C., Jaillais, Y., et al. (2020). Temporal integration of auxin information for the regulation of patterning. *eLife* **9**, e55832.

Gordon, S. P., Chickarmane, V. S., Ohno, C. and Meyerowitz, E. M. (2009). Multiple feedback loops through cytokinin signaling control stem cell number within the Arabidopsis shoot meristem. *Proc. Natl. Acad. Sci.* **106**, 16529–16534.

Goriely, A. (2017). *The Mathematics and Mechanics of Biological Growth*. New York, NY: Springer New York.

Gruel, J., Landrein, B., Tarr, P., Schuster, C., Refahi, Y., Sampathkumar, A., Hamant, O., Meyerowitz, E. M. and Jo nsson, H. (2016). An epidermis-driven mechanism positions and scales stem cell niches in plants. *Sci. Adv.* **2**, e1500989–e1500989.

Hardtke, C. S. and Berleth, T. (1998). The Arabidopsis gene MONOPTEROS encodes a transcription factor mediating embryo axis formation and vascular development. *EMBO J.* **17**, 1405–1411.

Heisler, M. G., Ohno, C., Das, P., Sieber, P., Reddy, G. V., Long, J. A. and Meyerowitz, E. M. (2005). Patterns of Auxin Transport and Gene Expression during Primordium Development Revealed by Live Imaging of the Arabidopsis Inflorescence Meristem. *Curr. Biol.* **15**, 1899–1911.

Hervieux, N., Dumond, M., Sapala, A., Routier-Kierzkowska, A.-L., Kierzkowski, D., Roeder, A. H. K., Smith, R. S., Boudaoud, A. and Hamant, O. (2016). A Mechanical Feedback Restricts Sepal Growth and Shape in Arabidopsis. *Curr. Biol.*

Hong, L., Dumond, M., Tsugawa, S., Sapala, A., Routier-Kierzkowska, A.-L., Zhou, Y., Chen, C., Kiss, A., Zhu, M., Hamant, O., et al. (2016). Variable Cell Growth Yields Reproducible Organ Development through Spatiotemporal Averaging. *Dev. Cell* **38**, 15–32.

Jeong, S., Trotochaud, A. E. and Clark, S. E. (1999). The Arabidopsis CLAVATA2 Gene Encodes a Receptor-like Protein Required for the Stability of the CLAVATA1 Receptor-like Kinase. *Plant Cell* **11**, 1925–1933.

Jönsson, H., Heisler, M., Reddy, G. V., Agrawal, V., Gor, V., Shapiro, B. E., Mjolsness, E. and Meyerowitz, E. M. (2005). Modeling the organization of the WUSCHEL expression domain in the shoot apical meristem. *Bioinforma. Oxf. Engl.* **21 Suppl 1**, i232-240.

Jönsson, H., Heisler, M. G., Shapiro, B. E., Meyerowitz, E. M. and Mjolsness, E. (2006). An auxin-driven polarized transport model for phyllotaxis. *Proc. Natl. Acad. Sci. U. S. A.* **103**, 1633–1638.

Kamimoto, K., Kaneko, K., Kok, C. Y.-Y., Okada, H., Miyajima, A. and Itoh, T. (2016). Heterogeneity and stochastic growth regulation of biliary epithelial cells dictate dynamic epithelial tissue remodeling. *eLife* **5**, e15034.

Kayes, J. M. and Clark, S. E. (1998). CLAVATA2, a regulator of meristem and organ development in Arabidopsis. *Development* **125**, 3843–3851.

Kiss, A., Moreau, T., Mirabet, V., Calugaru, C. I., Boudaoud, A. and Das, P. (2017). Segmentation of 3D images of plant tissues at multiple scales using the level set method. *Plant Methods* **13**,.

Klawe, F. Z., Stiehl, T., Bastian, P., Gaillochet, C., Lohmann, J. U. and Marciniak-Czochra, A. (2020). Mathematical modeling of plant cell fate transitions controlled by hormonal signals. *PLoS Comput. Biol.* **16**, e1007523.

Kulkarni, A. H., Chatterjee, A., Kondaiah, P. and Gundiah, N. (2018). TGF- β induces changes in breast cancer cell deformability. *Phys. Biol.* **15**, 065005.

Kwon, C. S., Chen, C. and Wagner, D. (2005). WUSCHEL is a primary target for transcriptional regulation by SPLAYED in dynamic control of stem cell fate in Arabidopsis. *Genes Dev.* **19**, 992–1003.

Laufs, P., Grandjean, O., Jonak, C., Kiêu, K. and Traas, J. (1998). Cellular parameters of the shoot apical meristem in Arabidopsis. *Plant Cell Online* **10**, 1375–1389.

Laux, T., Mayer, K. F., Berger, J. and Jurgens, G. (1996). The WUSCHEL gene is required for shoot and floral meristem integrity in Arabidopsis. *Development* **122**, 87–96.

Lenhard, M. and Laux, T. (2003). Stem cell homeostasis in the Arabidopsis shoot meristem is regulated by intercellular movement of CLAVATA3 and its sequestration by CLAVATA1. *Development* **130**, 3163–3173.

Lindsay, D. L., Sawhney, V. K. and Bonham-Smith, P. C. (2006). Cytokinin-induced changes in CLAVATA1 and WUSCHEL expression temporally coincide with altered floral development in Arabidopsis. *Plant Sci.* **170**, 1111–1117.

Long, J. A., Moan, E. I., Medford, J. I. and Barton, M. K. (1996). A member of the KNOTTED class of homeodomain proteins encoded by the STM gene of Arabidopsis. *Nature* **379**, 66–69.

Long, Y., Cheddadi, I., Mosca, G., Mirabet, V., Dumond, M., Kiss, A., Traas, J., Godin, C. and Boudaoud, A. (2020). Cellular Heterogeneity in Pressure and Growth Emerges from Tissue Topology and Geometry. *Curr. Biol.* **30**, 1504-1516.e8.

Luo, L., Zeng, J., Wu, H., Tian, Z. and Zhao, Z. (2018). A Molecular Framework for Auxin-Controlled Homeostasis of Shoot Stem Cells in Arabidopsis. *Mol. Plant* **11**, 899–913.

Ma, Y., Miotk, A., Šutiković, Z., Ermakova, O., Wenzl, C., Medzihradszky, A., Gaillochet, C., Forner, J., Utan, G., Brackmann, K., et al. (2019). WUSCHEL acts as an auxin response rheostat to maintain apical stem cells in Arabidopsis. *Nat. Commun.* **10**, 1–11.

Mayer, K. F., Schoof, H., Haecker, A., Lenhard, M., Jürgens, G. and Laux, T. (1998). Role of WUSCHEL in regulating stem cell fate in the Arabidopsis shoot meristem. *Cell* **95**, 805–815.

Medford, J. I., Behringer, F. J., Callos, J. D. and Feldmann, K. A. (1992). Normal and abnormal development in the Arabidopsis vegetative shoot apex. *Plant Cell* **4**, 631–643.

Milani, P., Gholamirad, M., Traas, J., Arnéodo, A., Boudaoud, A., Argoul, F. and Hamant, O. (2011). In vivo analysis of local wall stiffness at the shoot apical meristem in Arabidopsis using atomic force microscopy: Measuring wall stiffness in meristems with AFM. *Plant J.* **67**, 1116–1123.

Milani, P., Mirabet, V., Cellier, C., Rozier, F., Hamant, O., Das, P. and Boudaoud, A. (2014). Matching Patterns of Gene Expression to Mechanical Stiffness at Cell Resolution through Quantitative Tandem Epifluorescence and Nanoindentation. *PLANT Physiol.* **165**, 1399–1408.

Miwa, H., Betsuyaku, S., Iwamoto, K., Kinoshita, A., Fukuda, H. and Sawa, S. (2008). The Receptor-Like Kinase SOL2 Mediates CLE Signaling in Arabidopsis. *Plant Cell Physiol.* **49**, 1752–1757.

Müller, R., Borghi, L., Kwiatkowska, D., Laufs, P. and Simon, R. (2006). Dynamic and

Compensatory Responses of Arabidopsis Shoot and Floral Meristems to CLV3 Signaling. *Plant Cell* **18**, 1188–1198.

Müller, R., Bleckmann, A. and Simon, R. (2008). The Receptor Kinase CORYNE of *Arabidopsis* Transmits the Stem Cell–Limiting Signal CLAVATA3 Independently of CLAVATA1. *Plant Cell Online* **20**, 934–946.

Nemec-Venza, Z., Madden, C., Stewart, A., Liu, W., Novák, O., Pěnčík, A., Cuming, A. C., Kamisugi, Y. and Harrison, C. J. (2022). CLAVATA modulates auxin homeostasis and transport to regulate stem cell identity and plant shape in a moss. *New Phytol.* **234**, 149–163.

Nimchuk, Z. L., Tarr, P. T., Ohno, C., Qu, X. and Meyerowitz, E. M. (2011). Plant Stem Cell Signaling Involves Ligand-Dependent Trafficking of the CLAVATA1 Receptor Kinase. *Curr. Biol.* **21**, 345–352.

Plong, A., Rodriguez, K., Alber, M., Chen, W. and Reddy, G. V. (2021). CLAVATA3 mediated simultaneous control of transcriptional and post-translational processes provides robustness to the WUSCHEL gradient. *Nat. Commun.* **12**, 6361.

Popham, R. A. (1951). Principal Types of Vegetative Shoot Apex Organization in Vascular Plants. *Ohio J. Sci.* **51**, 249–269.

Posit team (2023). RStudio: Integrated Development Environment for R. Posit Software, PBC, Boston, MA. URL http://www.posit.co/.

Qiu, C., Dutcher, R. C., Porter, D. F., Arava, Y., Wickens, M. and Hall, T. M. T. (2019). Distinct RNA-binding modules in a single PUF protein cooperate to determine RNA specificity. *Nucleic Acids Res.* gkz583.

Reddy, G. V. and Meyerowitz, E. M. (2005). Stem-Cell Homeostasis and Growth Dynamics Can Be Uncoupled in the Arabidopsis Shoot Apex. *Science* **310**, 663–667.

Reinhardt, D., Mandel, T. and Kuhlemeier, C. (2000). Auxin Regulates the Initiation and Radial Position of Plant Lateral Organs. *Plant Cell* **12**, 507–518.

Routier-Kierzkowska, A.-L., Weber, A., Kochova, P., Felekis, D., Nelson, B. J., Kuhlemeier, C. and Smith, R. S. (2012). Cellular Force Microscopy for in Vivo Measurements of Plant Tissue Mechanics. *PLANT Physiol.* **158**, 1514–1522.

Schillers, H., Rianna, C., Schäpe, J., Luque, T., Doschke, H., Wälte, M., Uriarte, J. J., Campillo, N., Michanetzis, G. P. A., Bobrowska, J., et al. (2017). Standardized Nanomechanical Atomic Force Microscopy Procedure (SNAP) for Measuring Soft and Biological Samples. *Sci. Rep.* **7**,.

Schindelin, J., Arganda-Carreras, I., Frise, E., Kaynig, V., Longair, M., Pietzsch, T., Preibisch, S., Rueden, C., Saalfeld, S., Schmid, B., et al. (2012). Fiji: an open-source platform for biological-image analysis. *Nat. Methods* **9**, 676–682.

Schlegel, J., Denay, G., Wink, R. H., Pinto, K. G., Stahl, Y., Schmid, J., Blümke, P. and Simon, R. G. (2021). Control of Arabidopsis shoot stem cell homeostasis by two antagonistic CLE

peptide signalling pathways. *eLife* **10**, e70934.

Schoof, H., Lenhard, M., Haecker, A., Mayer, K. F. X., Jürgens, G. and Laux, T. (2000). The Stem Cell Population of Arabidopsis Shoot Meristems Is Maintained by a Regulatory Loop between the CLAVATA and WUSCHEL Genes. *Cell* **100**, 635–644.

Schuster, C., Gaillochet, C., Medzihradszky, A., Busch, W., Daum, G., Krebs, M., Kehle, A. and Lohmann, J. U. (2014). A Regulatory Framework for Shoot Stem Cell Control Integrating Metabolic, Transcriptional, and Phytohormone Signals. *Dev. Cell* **28**, 438–449.

Shapiro, B. E., Tobin, C., Mjolsness, E. and Meyerowitz, E. M. (2015). Analysis of cell division patterns in the *Arabidopsis* shoot apical meristem. *Proc. Natl. Acad. Sci.* **112**, 4815–4820.

Taguchi-Shiobara, F. (2001). The fasciated ear2 gene encodes a leucine-rich repeat receptor-like protein that regulates shoot meristem proliferation in maize. *Genes Dev.* **15**, 2755–2766.

Tam, P. P., Barrette-Ng, I. H., Simon, D. M., Tam, M. W., Ang, A. L. and Muench, D. G. (2010). The Puf family of RNA-binding proteins in plants: phylogeny, structural modeling, activity and subcellular localization. *BMC Plant Biol.* **10**, 44.

Tsugawa, S., Hervieux, N., Kierzkowski, D., Routier-Kierzkowska, A.-L., Sapala, A., Hamant, O., Smith, R. S., Roeder, A. H. K., Boudaoud, A. and Li, C.-B. (2017). Clones of cells switch from reduction to enhancement of size variability in Arabidopsis sepals. *Development* **144**, 4398–4405.

Tvergaard, V. and Needleman, A. (2018). Effect of Properties and Turgor Pressure on the Indentation Response of Plant Cells. *J. Appl. Mech.*

Vernoux, T., Kronenberger, J., Grandjean, O., Laufs, P. and Traas, J. (2000). PIN-FORMED 1 regulates cell fate at the periphery of the shoot apical meristem. *Development* **127**, 5157–5165.

Vernoux, T., Brunoud, G., Farcot, E., Morin, V., Van den Daele, H., Legrand, J., Oliva, M., Das, P., Larrieu, A., Wells, D., et al. (2011). The auxin signalling network translates dynamic input into robust patterning at the shoot apex. *Mol. Syst. Biol.* **7**, 508.

Whitewoods, C. D., Cammarata, J., Nemec Venza, Z., Sang, S., Crook, A. D., Aoyama, T., Wang, X. Y., Waller, M., Kamisugi, Y., Cuming, A. C., et al. (2018). CLAVATA Was a Genetic Novelty for the Morphological Innovation of 3D Growth in Land Plants. *Curr. Biol.*

Wu, X., Dabi, T. and Weigel, D. (2005). Requirement of Homeobox Gene STIMPY/WOX9 for Arabidopsis Meristem Growth and Maintenance. *Curr. Biol.* **15**, 436–440.

Yadav, R. K., Girke, T., Pasala, S., Xie, M. and Reddy, G. V. (2009). Gene expression map of the Arabidopsis shoot apical meristem stem cell niche. *Proc. Natl. Acad. Sci.* **106**, 4941–4946.

Yadav, R. K., Perales, M., Gruel, J., Girke, T., Jönsson, H. and Reddy, G. V. (2011). WUSCHEL protein movement mediates stem cell homeostasis in the Arabidopsis shoot apex. *Genes Dev.* **25**, 2025–2030.

Yamaguchi, N., Wu, M.-F., Winter, C. M., Berns, M. C., Nole-Wilson, S., Yamaguchi, A., Coupland, G., Krizek, B. A. and Wagner, D. (2013). A molecular framework for auxin-

mediated initiation of flower primordia. *Dev. Cell* **24**, 271–282.

Zhao, Z., Andersen, S. U., Ljung, K., Dolezal, K., Miotk, A., Schultheiss, S. J. and Lohmann, J. U. (2010). Hormonal control of the shoot stem-cell niche. *Nature* **465**, 1089–1092.

Figure 1

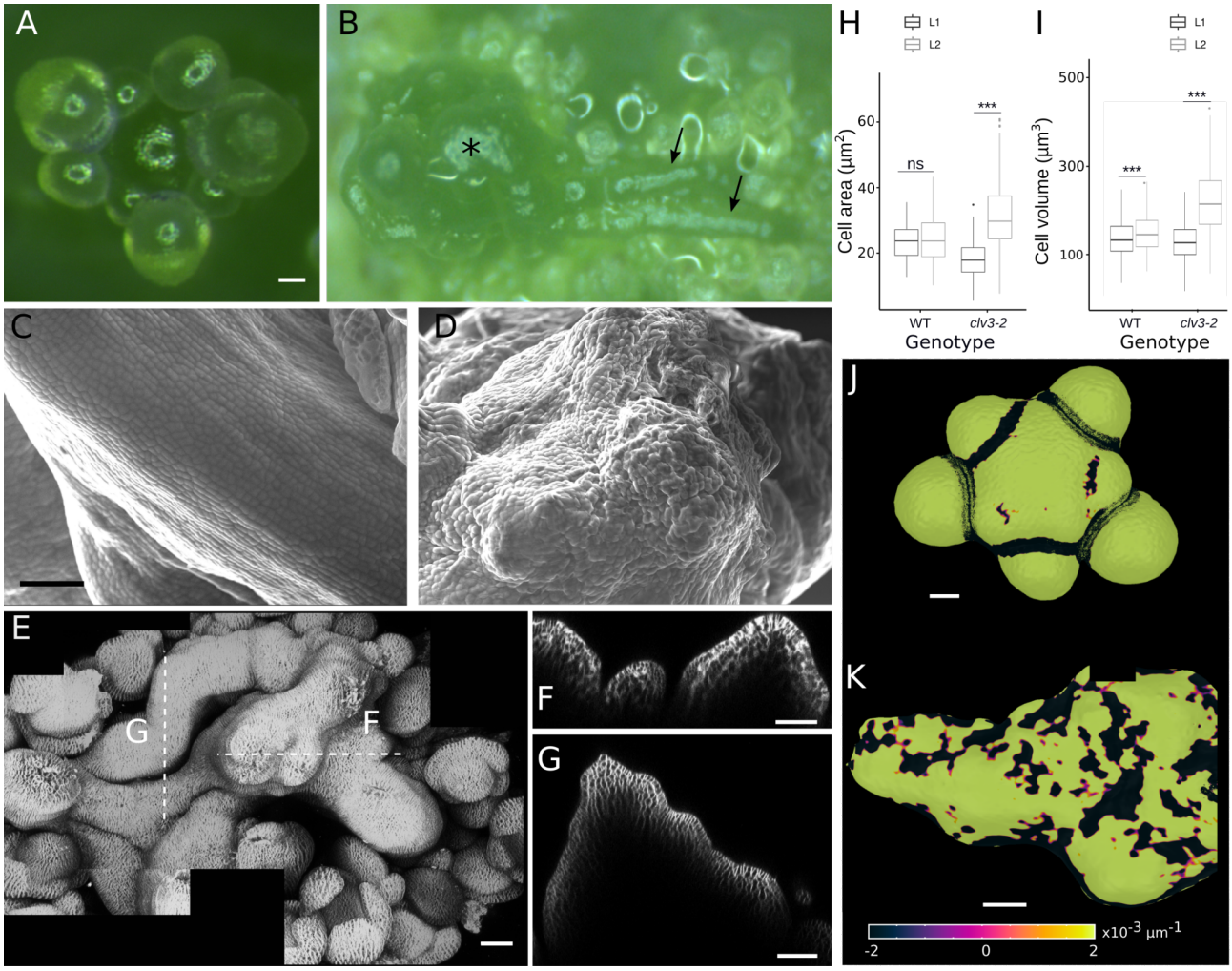

Figure 1. Altered cell and tissue properties characterise fasciated SAM

(A, B) Bright field images showing dissected WT (A) and *clv3-2* (B) SAM. The asterisk in (B) shows the central outgrowth and arrows point out two linear elongations. **(C, D)** SEM images showing cell organisation in the linear part of a *clv3-2* SAM (C), and at the top of an outgrowth (D). **(E-G)** Maximum intensity projection of a 3D confocal stack showing a *clv3-2* fasciated SAM. Cell membranes are stained with FM4-64. Dashed lines represent orthogonal sections shown in (F, G), through elongated areas and an outgrowth, respectively. **(H)** Boxplots of cell area in the L1 (black) and L2 (grey) cell layers of WT and *clv3-2* SAM. Mean ± s. d. areas are 23.9 ± 5.83 µm^2 for WT L1, 24.5 ± 7.18 µm^2 for WT L2, 18.4 ± 5.34 µm^2 for *clv3-2* L1, and 31.2 ± 9.84 µm^2 for *clv3-2* L2. L1 and L2 cells have significantly different areas in *clv3-2* mutants (Welch's t-test,, p = 4.65e-54) but not in WT plants (Welch's t-test, p = 0.545). n = 103 (L1) and 115 (L2) cells from 3 WT SAM, 400 (L1) and 244 (L2) cells from 3 *clv3-2* SAM. **(I)** Boxplots of cell volumes within the L1 (black) and the L2 (grey) cell layers of WT and *clv3-2* SAM. Outliers are not shown. Mean ± s. d. volumes are 136.51 ± 40.45 µm^3 for WT L1, 148.72 ± 44.54 µm^3 for WT L2, 129.48 ± 40.86 µm^3 for *clv3-2* L1, and 249.08 ± 130.65 µm^3 for *clv3-2* L2. L1 and L2 cells have significantly different volumes in WT (Welch's t-test, p = 2.32e-9)

and c*lv3-2* (Welch's t-test, p = 1.53e-204), but the general trend observed is that in *clv3-2*, cell volumes in the L2 are much greater than in the L1, whereas in the WT the two layers show similar cell volume values. n= 1468 L1 cells and 529 L2 cells from 4 WT SAM; 6426 L1 cells and 3428 L2 cells from 3 *clv3-2* SAM. Scale bars = 100 µm (A), 20 µm (B). **(J, K)** Colour maps quantifying the local curvature in a WT (J) and a *clv3-2* (K) SAM. Only a fragment of the mutant SAM is shown in (K) due to very large fasciation. Colour scale in μm^{-1}. Scale bars: 30 µm (A, B, shown in A), 25 µm (C, D, shown in C), 50 µm (E-G, K), 20 µm (J).

Figure 2

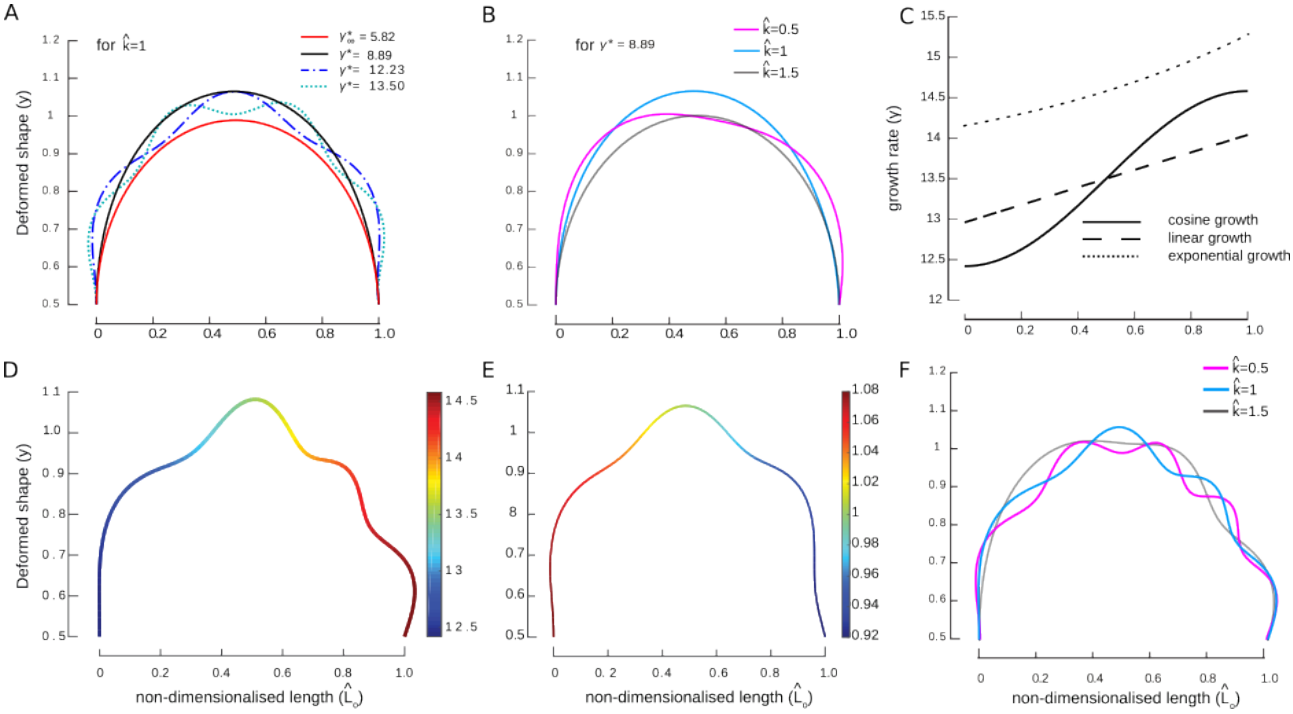

Figure 2. Growth and stiffness influence SAM shapes via growth-induced buckling

(A) Deformed shapes due to growth-induced buckling obtained for different values of critical growth rates (γ*) causing various buckling modes, with the stiffness of the underlying foundation fixed ($\hat{k}$=1). **(B)** Deformed shapes due to stiffness-induced buckling obtained for different values of foundation stiffness ($\hat{k}$=0.5, 1, 1.5), with the growth rate fixed (γ*=8.99). **(C)** The choice of growth law affects the deformed shapes. We select three different forms of growth laws for the same value of growth rate γ_0 - cosine, linear and exponential. **(D)** Deformed shape obtained as a result of growth-induced buckling in the case of cosine growth distribution. **(E)** Deformed shape obtained as a result of stiffness-induced buckling in the case of cosine stiffness distribution. **(F)** Effect of foundation stiffness on the asymmetric rod shapes obtained using growth heterogeneity.

Figure 3

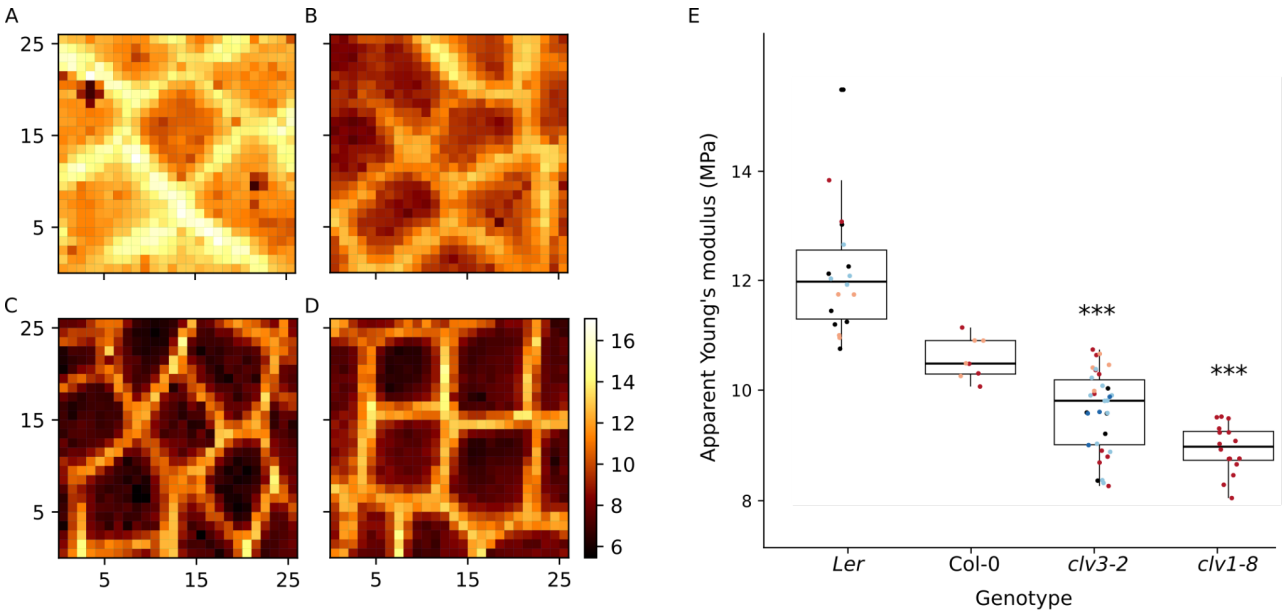

Figure 3. Loss of *clv* is associated with a reduction in epidermal cell stiffness

(A-D) Representative apparent Young's modulus maps of L*er* (A), Col-0 (B), *clv3-2* (C), and *clv1-8* (D) SAM. The colour scale quantifies the apparent Young's modulus (MPa). x, y axis: pixel number. **(E)** Box plots of mean apparent Young's moduli (MPa) measured on epidermal cells of L*er* (n=11), Col-0 (n=2), *clv3-2* (n=8), and *clv1-8* (n=1) SAM. Mean ± s. d. values are 12.16 ± 1.17 MPa for L*er*, 9.63 ± 0.74 MPa for *clv3-2*, 10.58 ± 0.38 MPa for Col-0, 8.94 ± 0.45 MPa *clv1-8*. On average, *clv3-2* and *clv1-8* have significantly lower apparent Young's moduli than the WT (L*er* for *clv3-2*, and Col-0 for *clv1-8*, respectively), as represented by *** (Welch's t-test, p=6.65e-8, p=1.85e-7 respectively). Black dots: each dot represents the mean apparent Young's modulus of a single sample; coloured dots: one colour represents a single sample for which several non-overlapping acquisitions were made, each dot shows the mean apparent Young's modulus per acquisition.

Figure 4

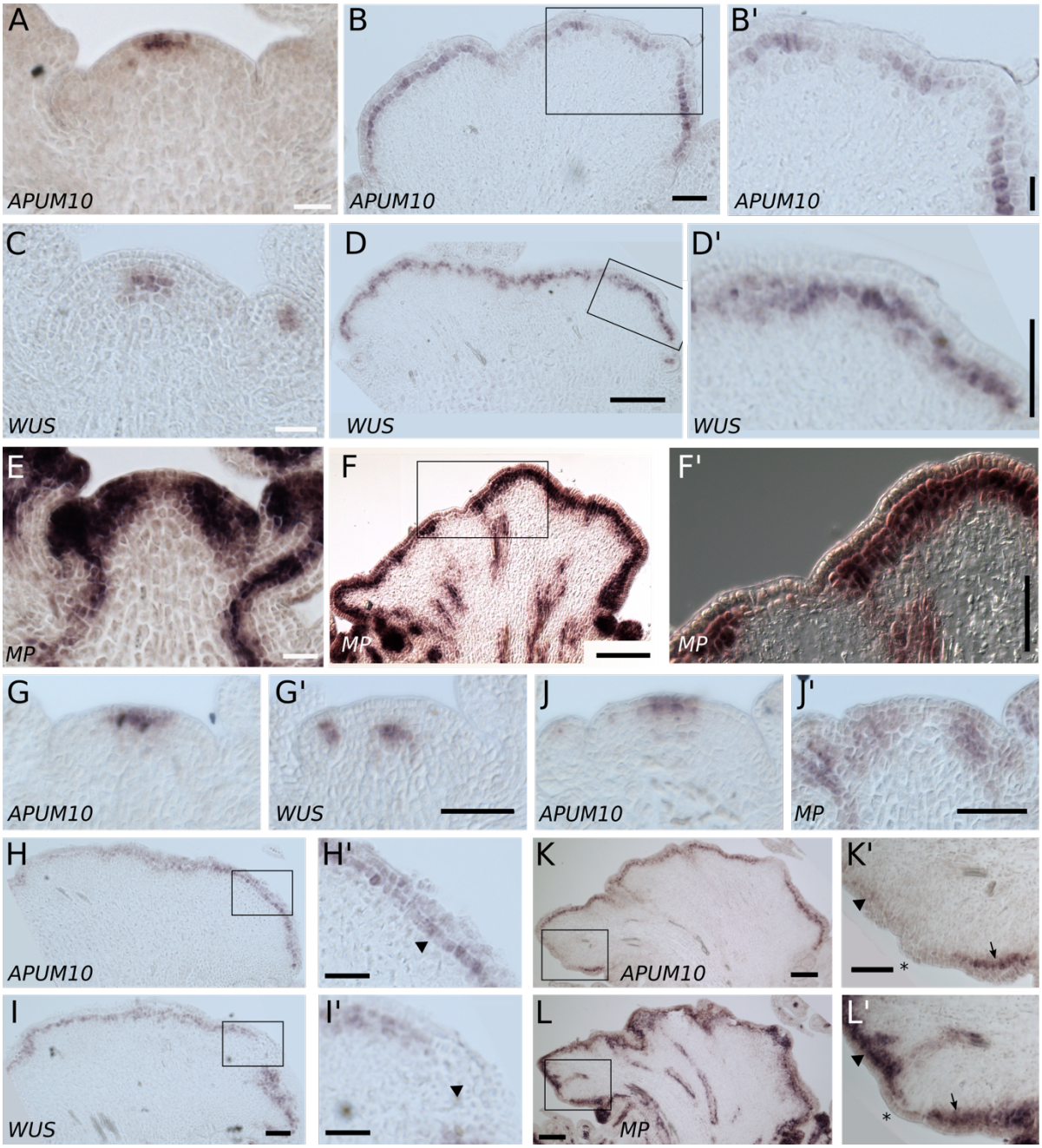

Figure 4. Gene expression is heterogenous in *clv3* SAM

(A-F') RNA *in situ* hybridisation of probes *APUM10* (A-B'), *WUS* (C-D'), and *MP* (E-F') on WT (A, C, E) and *clv3-2* (B, B', D, D', F, F') SAM. (B', D', and F') are close ups of the regions boxed in (B, D, and F), respectively. **(G-L')** *APUM10* (G, J, H, H', K, K'), *WUS* (G', I, I'), and *MP* (J', L, L') probes hybridised on consecutive sections of a single WT (G, G', J, J') or *clv3-2* (H-I', K-L') SAM. In (H',I'), arrowheads point to zones where *APUM10* mRNA is detected but not that of *WUS*. In (K', L'), arrowheads point to zones where *MP* mRNA is detected but not that of *APUM10*, asterisks show areas without *APUM10* nor *MP* probe detection, and arrows represent zones where both probes are detected. (H', I', K', and L') are close ups of the boxed areas shown in (H, I, K, and L), respectively. Section thickness: 10 µm. Scale bars: 50 µm (A, B', C, D', E, F', G, G', H', I', J, J', K', L'), 100 µm (B, D, F, H, I, K, L).

Figure 5

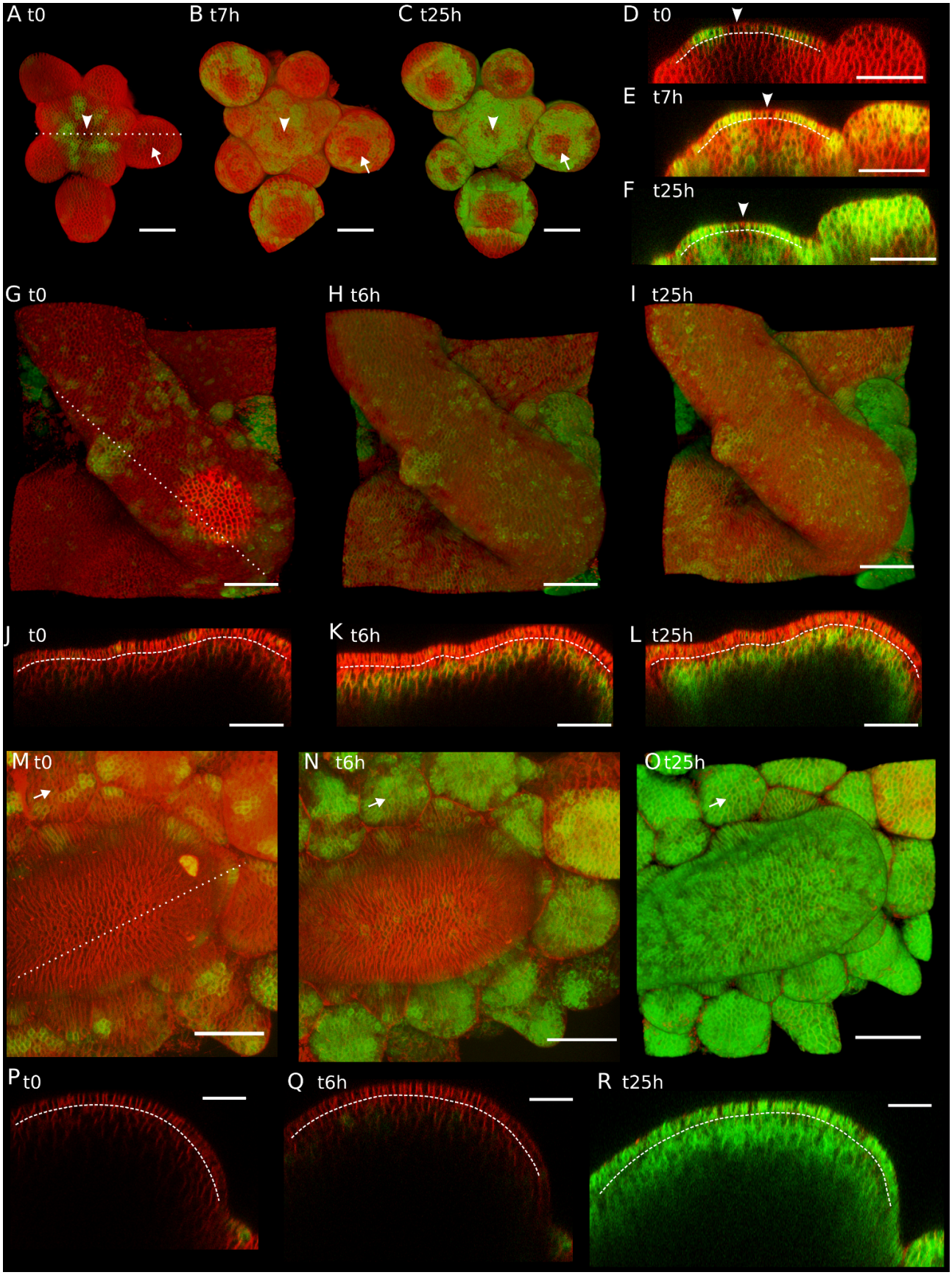

Figure 5. *clv3* meristematic cells strongly respond to exogenous auxin

Projections of confocal stacks showing the effect of 1 mM IAA exogenous treatment on WT **(A-F)** and *clv3-2* **(G-R)** SAM expressing the *DR5::GFPer* reporter. The pictures show samples before treatment (A, D, G, J, M, P), 6 or 7 hours (B, E, H, K, N, Q), and 25 hours (C, F, I, L, O, R) after the 5-hour IAA treatment. (G-L) *clv3-2* SAM representative of the first group of responses to IAA (n=4/6). (M-R) *clv3-2* SAM representative of the second group of responses to IAA (n=2/6). Orthogonal views of the SAM in (D-F, J-L, P-R) are taken along the dotted lines shown in (A, G, M), respectively. Arrowheads in (A-F) indicate the centre of the SAM, arrows in (A-C, M-O) show representative flowers, and dashed lines in orthogonal sections represent the interface between L1 and L2 layers. Scale bars: 50 µm (A-O), 30 µm (P-R). n = 7 WT SAM, n = 6 *clv3-2* SAM. This experiment was replicated four times in the laboratory.